NEWLY FORMED SEA ICE IN ARCTIC LEADS MONITORED BY C- AND L-BAND SAR

A. Malin Johansson[1,*], Camilla Brekke[1], Gunnar Spreen[2,3], Jennifer A. King[3], and Sebastian Gerland[3]

[1] *UiT The Arctic University of Norway, Department of Physics and Technology, NO-9037, Tromsø, Norway*
[2] *University of Bremen, Institute of Environmental Physics, D-28359 Bremen*
[3] *Norwegian Polar Institute, Fram Centre, NO-9296 Tromsø, Norway*
[*] *E-mail: malin.johansson@uit.no*

ABSTRACT

We investigate the scattering entropy and co-polarization ratio for Arctic lead ice using C- and L-band synthetic aperture radar (SAR) satellite scenes. During the Norwegian Young sea ICE (N-ICE2015) cruise campaign overlapping SAR scenes, helicopter borne sea ice thickness measurements and photographs were collected. We can therefore relate the SAR signal to sea ice thickness measurements as well as photographs taken of the sea ice. We show that a combination of scattering and co-polarization ratio values can be used to distinguish young ice from open water and surrounding sea ice.

Key words: Sea ice, SAR.

1. INTRODUCTION

Under calm conditions newly formed thin ice can have a backscatter signal comparable to oil spills and low wind areas in synthetic aperture radar (SAR) imagery. Hence, in case of an oil spill accident newly formed thin sea ice could be seen as an oil spill look-alike. Given the predicted increase in maritime activities in the Arctic Ocean [2] it is important to be able to separate thin ice from oil spills. The good spatial coverage and high temporal resolution means that medium spatial resolution C-band SAR data such as Radarsat-2 and Sentinel-1 Wide Swath has been favoured for operational near-real time deliver of sea-ice information. C-band SAR is used by the European Maritime Safety Agency (EMSA) for detection of oil spills in the European part of the Arctic ocean. SAR satellites offer the opportunity to monitor the Artic Ocean on a daily basis as they are not hindered by cloud cover nor by lack of daylight. Newly formed sea ice often form in openings in the sea ice, so called leads. These leads are, even when covered with a thin ice layer, important areas of heat fluxes from the underlying water to the atmosphere.

From January to June 2015 the Norwegian Young sea ICE (N-ICE2015) cruise campaign was carried out by the Norwegian Polar Institute and partner institutes in the sea ice north of Svalbard. One of the goals for this campaign was to study the changed Arctic sea ice regime of primarily seasonal ice and also the growth of new ice. The latter was important for this study as it meant that substantial *in-situ* information was collected during the transition period from the Arctic winter polar nights and the melt season. The *in-situ* data includes electro-magnetic (EM) soundings and ground measurements of sea ice thickness and salinity. Co-located C- and L-band SAR scenes were obtained that are co-incident with these *in-situ* measurements.

Studies by, [20] and [21] showed that scattering entropy can be used to successfully distinguish newly formed ice from open water. However, their study area, the Okhotsk Sea, has different sea ice conditions than our study region north of Svalbard with the majority of the sea ice consisting of less than 1 meter thick first year ice [21]. North of Svalbard the sea ice cover was predominantly first-year sea ice (FYI) with multiyear ice (MYI) floes enclosed within [11].

Co-polarization ratios were successful used by e.g. [1], [22], [6], [7], [10], [12], [3] and [18] to identify young ice. High absolute co-polarisation ratio values have been used to separate newly formed ice from the surrounding sea ice in X-, C- and L-band. In [6] they identified that thin ice was easier to distinguish in L-band data than in X- and C- band data. By using simulated ALOS Phased-Array type L-band (Palsar) data [7] showed that the co-polarisation ratio could be used to identify new and young ice. Using C-band data with an incidence angle of 30^o-45^o [7] also identified that the new ice may be difficult to distinguish from first-year and multi-year ice due to the noise floor level.

In [3] they used the co-polarization ratio for C-, X- and Ku-band to classify nilas, grey ice, open water and old ice. In [10] they successfully classified multi-year ice, first year ice, thin ice and open water using C-band SAR co-polarization ratios, finding that thin ice showed more variation in the co-polarization ratio than first year ice and multi-year ice. Using the time series of co-located satellite scenes from N-ICE2015 we aim to study such variations more closely. Once an opening in the form of

cracks and leads has started the process of new ice formation may begin. For the scenes used in this study the temperatures range from -22^oC to -3.5^oC. Hence, different temperature conditions can be investigated and with temperatures down to -22^{o}C new ice formation could take place.

We focus our study on thin ice located in refrozen leads, about which we have obtained a significant volume of *in-situ* data. We compare two different parameters; scattering entropy and co-polarization ratio for overlapping C- and L-band imagery and how they vary with frequency and sea ice thickness.

1.1. Data collection

1.1.1. Satellite scenes

In this study, we use Radarsat-2 Quad polarimetric Fine (Radarsat-2) scenes and ALOS-2 Palsar-2 Stripmap Full Polarization (ALOS-2) scenes (Tab. 1). The scenes were collected during April and May 2015. The scenes cover different areas but all are located within a bounding box from 80^{o}N to 84^{o}N and 0^{o}E to 20^{o}E (Fig. 1).

In total five different C- and L-band image pairs were used in this study (Tab. 3). For all pairs, the two satellite acquisitions were taken on the same day but with a time gap between them. Care was taken to select scenes with minimum possible time gap between them. The noise equivalent sigma zero (NESZ) which is the background noise (noise floor) is presented in Tab. 3. The L-band scenes have a satellite sensor specific NESZ of -41.1 dB. For the C-band scenes the NESZ values are scene specific and calculated using the mean incidence angle.

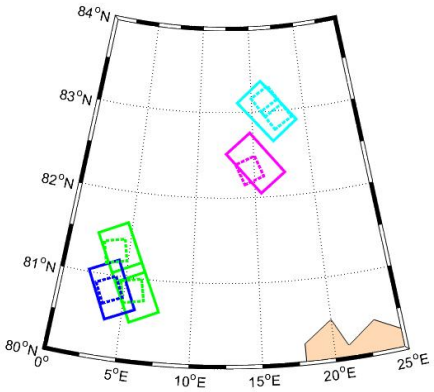

Figure 1: Satellite scene areal extent where the solid lines indicate the L-band scenes and the dotted lines the C-band scenes. Cyan color indicate scenes from 23 April, magenta scenes from 28 April, green scenes from 26 May and blue scenes from 31 May 2015. The coast line in the south east of the map represents the north-eastern part of Svalbard.

Table 1: Properties of the satellite scenes

Mission	Radarsat-2	ALOS-2
Frequency band	C (5.41 GHz)	L (1.2 GHz)
Acquisition mode	Polarimetric Fine	Stripmap Full Polarization
Polarization	Quad	Quad
HH, HV, VH, VV		
Pass mode	Ascending	Ascending
Range resolution*	5.2 m	5.1 m
Az. resolution*	7.6 m	4.3 m
Width	27 km	40-50 km
Length	35 km	70 km
	*Nominal values	

1.1.2. *In-situ* measurements

In this study we make use of helicopter-borne EM induction soundings, henceforth referred to as HEM measurements (for the method see [13], [17]). HEM total (ice and snow) thickness surveys with accompanying photographs were located within the satellite scenes areal extent. Downward-looking photographs were taken with a GoPro camera (model YHDC5170) every two seconds. The photographs were used to extract visual information about the sea ice surface, e.g. snow cover, presence of frost flowers, rafting and ridges. The footprints of the HEM measurements are ∼40–50 m and the photographs have a similar foot print. Two co-located HEM flights are used in this study, 24 April and 28 April (Tab. 2).

R/V Lance was moored to one sea ice floe from 18 April to 5 June 2015 and drifted with the ice. Meteorological observations were collected aboard R/V Lance every 30 seconds at 22 m a.s.l. (Tab. 3) as well as accurate positioning data every second.

Table 2: HEM flight specifications.

Date	Start time (UTC)	Stop time (UTC)
2015-04-24	14:24	15:27
2015-04-28	07:24	08:23

2. STUDY AREA

The study area is located in the Arctic Ocean north of Svalbard (Fig. 1). This region covers the transition from the shallower shelf and Yermak Plateau north of Svalbard to the deep Arctic Basin further north. In-situ data from the N-ICE2015 drift study reveals that the ice cover was predominantly first-year sea ice (FYI) with multiyear ice (MYI) floes enclosed within [11]. Observations and *in-situ* measurement show that there are also areas of e.g. nilas, young grey ice and pancake ice. The majority of the young ice was found in re-frozen leads during the time period and area considered here.

Table 3: Properties of the SAR scenes used in this study. The meteorological data is measured aboard R/V Lance at 22 m a.s.l. and are averaged over a 10–minute time period centred around the time of the satellite image acquisitions.

Pair #	Satellite	Date	Time (UTC)	Incidence angle (^{o})	Multi-looking	NESZ (dB)	Air temperature (^{o}C)	Wind speed (m/s)
1	Radarsat-2	2015-04-23	14:42	36.5 - 38.0	5 x 7	-31.96	-21.72	11.21
	ALOS-2	2015-04-23	20:18	32.4 - 35.4	7 x 11	-41.1	-18.52	7.81
2	Radarsat-2	2015-04-28	15:36	42.0 - 43.3	6 x 8	-31.78	-12.79	9.20
	ALOS-2	2015-04-28	20:25	29.5 - 32.6	7 x 11	-41.1	-13.18	7.90
3 & 4	Radarsat-2	2015-05-26	17:00	48.4 - 49.5	6 x 8	-30.08	-3.50	12.21
	ALOS-2	2015-05-26	22:02	37.7 - 40.3	8 x 12	-41.1	-4.54	12.25
5	Radarsat-2	2015-05-31	16:14	37.5 - 38.9	5 x 8	-32.48	-5.09	9.70
	ALOS-2	2015-05-31	22:08	37.7 - 40.3	8 x 12	-41.1	-6.30	8.53

3. METHOD AND DATA PROCESSING

3.1. Satellite data processing

For consistency, all satellite scenes were processed in the same way: Firstly, the scenes were radiometrically calibrated using the included metadata calibration information. Secondly, the satellite scenes were multi-looked to a ground square pixel size of approximately 40 m x 40 m. This size was chosen to overlap with the size of the HEM footprint. The different SAR scenes have different ground resolution therefore they were multi-looked using different number of looks (see Tab. 3). Care was taken to check the NESZ values so that areas below the NESZ were removed from the analysis.

The newly formed young thin ice was identified in the scenes using a mask. The mask was generated using the "extended polarimetric feature space" (EPFS) segmentation method described in [8] and [9]. The segment decision is based upon both polarimetric and textural information, and groups all pixels with similar statistical properties in the same cluster. The number of segments was determined automatically by the statistical goodness-of-fit of the modelling during the segmentation stage. The method has previously been shown to give good results on sea ice (e.g. [15]). The segmented areas were classified by a sea ice classification specialist at the Operational Ice Service of the Norwegian Meteorological Institute. Segments positively identified as young ice were then masked out from the surrounding sea ice. Young ice fraction was calculated as percentage of the total number of pixels within each scene.

For the feature analysis the co-polarization ratio was calculated as;

$$\text{Co-polarization} = \frac{Sigma_{VV}}{Sigma_{HH}} \tag{1}$$

The scattering entropy (H) was calculated as;

$$H = -\sum_{i=1}^{d} p_i log_d p_i \tag{2}$$

where d is the polarimetric dimension, λ_i are the quad-polarimetric eigenvalues and p_i=λ_i / (λ_1 + λ_2 + λ_3). The scattering entropy is one part of the H/A/α decomposition [4], where A is the anisotropy.

The α was calculated as;

$$\alpha = \sum_{i=1}^{3} p_i \alpha_i \tag{3}$$

3.2. Sea ice thickness measurements

The HEM system, hanging below the helicopter, takes advantage of the fact that sea ice has low electrical conductivity (conductivity range 0–50 mS/m) while sea water is a very good conductor (conductivity range 2400–2700 mS/m) [13]. The primary EM field generated by the transmitting coil of the system induces eddy currents in the sea water; the strength of the secondary EM field induced by these currents is measured by the receiving coil. The strength of the secondary EM field is related by an empiric calibration curve to the distance between the instrument and the sea water [13]. Having thus found the distance to water, a laser altimeter is used to find the distance to the ice or snow surface. The difference between the two is the total ice and snow thickness, henceforth referred to as ice thickness. The nominal uncertainty for a single measurement is 10 cm for level ice, with significantly larger errors occurring in heavily ridged areas [13]. The footprint of the HEM system is approximately $\sim$40–50 m.

3.3. Time separation adjustment

Due to the time separation between the satellite scenes and the HEM flights one fixed time was chosen for the different dates to correct all other data to; i.e. for 23 April the scenes and the HEM flights were shifted to 20:18 UTC (Fig. 2) and for 28 April the data were shifted to 20:25. No co-located flights were available for the two image pairs in May.

Given the high sea ice concentration and observations of the behaviour of the sea ice around R/V Lance we assume that the sea ice in the vicinity of R/V Lance is moving more or less in the same configuration as the vessel. There are some local scale relative movements of floes only in areas where open water or thin ice is present. We can therefore make use of the high accuracy positioning data from the research vessel to co-locate the scenes and the HEM flight track by moving the HEM data from the position it was acquired in to the position the same ice would have occupied at the time of the satellite image chosen as the fixed base for all co-locations. However, the alignment of the HEM flight lines to the satellite scenes is difficult and small scale local non-alignments may occur. Following an initial shift in position based on the ships track, the position of the HEM data was manually adjusted based on features visible in the relevant satellite image.

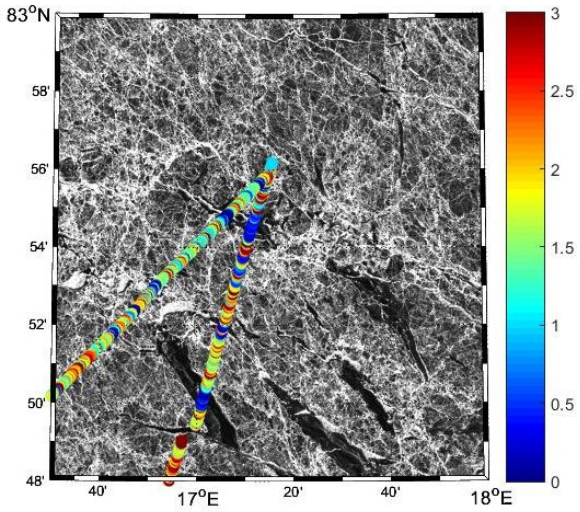

Figure 2: HEM flight overlapping the ALOS-2 L-band scene from April 23 2015. The colorbar shows the total snow and ice thickness.

4. RESULTS AND DISCUSSION

The relative occurrence of young ice within each satellite scene is given in Tab. 4. It should be noted that the satellite scenes do not have exactly the same areal extent; and that the dataset for April 23 and May 26 are made up of more than one individual satellite scene (Fig. 1).

Table 4: Young ice fraction as a part of the whole satellite scenes given in %. For May 26 two satellite scene pairs are used and they are denoted lower (L) and upper (U) referring to the respective scene pairs position as seen in Fig. 1. In Fig. 2 the areal extent of the satellite scenes are seen in cyan (2015-04-23), magenta (2015-04-28), green (2015-05-26) and blue (2015-05-31).

Date	Radarsat-2	ALOS-2
2015-04-23	12.3 and 15.2	15.1
2015-04-28	5.3	6.0
2015-05-26 (L)	7.2	8.2
2015-05-26 (U)	2.8	4.8
2015-05-31	3.5	6.5

Observations from R/V Lance show that between April 19 and April 24 a period of strong winds led to ice deformation and movement in the region adjacent to the ship; creating new openings in the form of cracks and leads. The situation stabilised and new ice began to form in the newly opened leads. New ice was blown to the downwind side of the wider openings, leaving open water on the upwind side for a lead close to R/V Lance. By 24 April the wind calmed down and ice could form on the remaining part of the lead. These environmental conditions explain the larger young ice fraction on April 23 than on April 19 (not shown here). Sea ice charts from the Ice Service of the Norwegian Meteorological Institute show >90% sea ice concentration in the study area on April 19 and areas with an ice concentration of >60% for April 23. We caveat this with the reminder that the areas observed for the individual days are not the same and hence the sea ice conditions may differ. Overall the fraction of young ice is higher (+1.6%) in the L-band scenes than the C-band scenes. One reason for this may be the longer wavelength for the L-band SAR compared to the C-band SAR. The difference in wavelength implies that the longer wavelength can correctly classify young ice (i.e. less than 30 cm in thickness) due to the higher penetration depth at L-band. Moreover, the backscatter intensity range was greater in the L-band data than the C-band data and this may be one of the reasons for the easier separation into distinct segments used for the young ice masking. This may be particularly important during the onset of melting where [5] argue that the longer wavelength in L-band SAR may render it less sensitive to the onset of melting.

We found that the backscatter signal differs between the C- and L-band imagery and that this is reflected both in the scattering entropy and the co-polarization ratio (Fig. 3). In Tab. 5 the mean values for all the young ice class within the individual scenes are presented.

In the C-band scenes the mean co-polarization ratio of the young ice is negative for April 23 and positive for the other four scenes (Tab. 5). The overlap between the HEM measurements and the C-band scenes on April 23 includes 3 wider leads clearly identifiable in both the

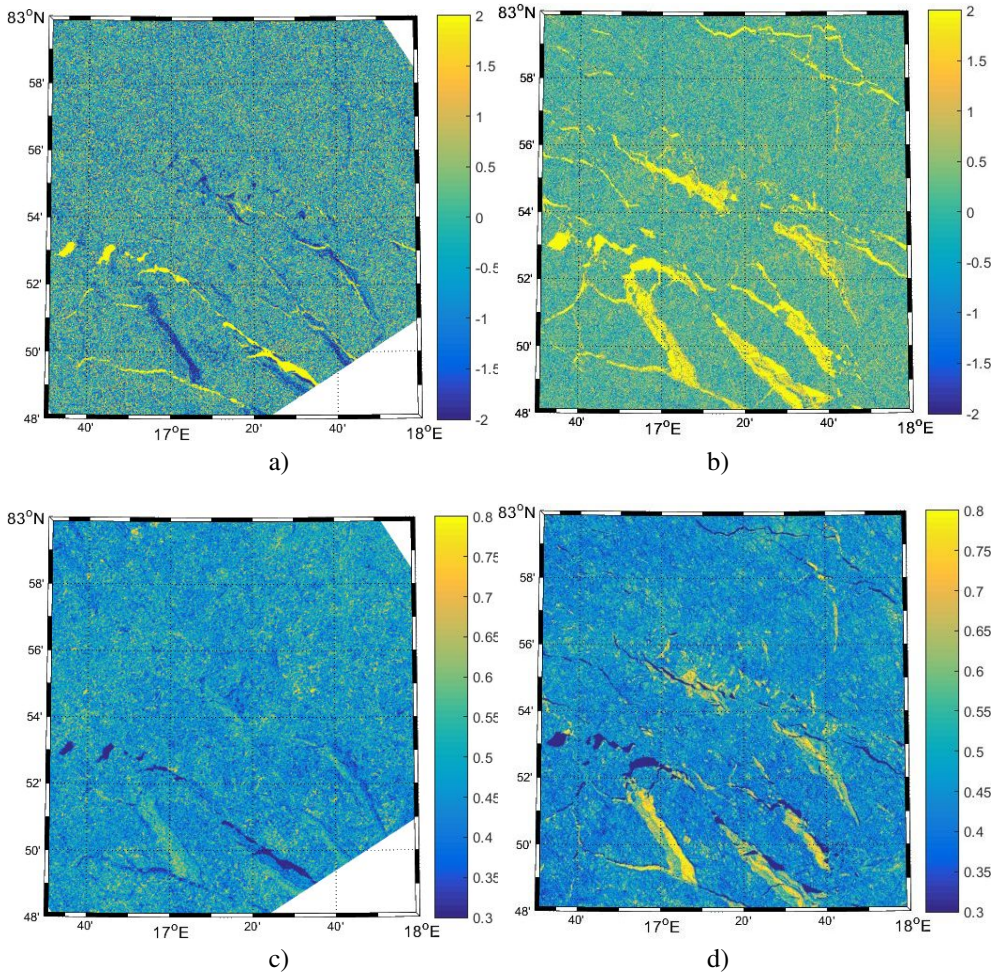

Figure 3: Co-polarization ratio in dB on April 23 in a) C-band and b) L-band. Scattering entropy on April 23 in c) C-band and d) L-band.

HEM measurements and the satellite scenes (Fig. 2). These leads were classified as open water/newly formed sea ice areas or young ice areas. Both types of segments have been included in our young ice class. The leads have typically values of $\sim$-2 dB and $\sim$2 dB. The distribution of the two types of leads are approximately 50% of each and explains the mean co-polarization value of 0.19 dB on April 23. Photographs from HEM flight show that the leads were both leads with young ice as well as open water. In the leads with open water the wind speeds (Tab. 3) were high enough to generate ripple waves on the surface visible in the photographs. These open water leads have co-polarization values of $\sim$2 dB. Additional narrow leads with values of $\sim$2 dB have newly formed level ice. The time separation between the satellite image acquisition and the HEM flight ($\sim$24 hours) means it is possible that these leads may not have been refrozen at the time of the satellite image acquisition. From the photographs it may be interpreted that these leads are younger than the other leads with lower co-polarization ratio ($\sim$-2 dB). Note that the actual thickness cannot be interpreted from the photographs but the relative thickness between two set of photographs may be inferred. For the leads with $\sim$-2 dB we observe thicker young ice. For these leads the HEM measurements indicate a thickness of 0.2 m. Note that the accuracy for the HEM measurements is 0.1 m over level sea ice. It is therefore not possible to accurately measure sea ice with a thickness below 0.1 m. The footprint of $\sim$40-50 m means that some measurements made over the thin ice will contain also the influence of the thicker ice adjacent to the leads. Photographs from one of these wider young ice lead show that the lead is divided into two parts; the first part is deformed young ice with frost flowers and the second part is level young ice with frost flowers. In the area with level young ice the co-polarization ratio is -2 dB and for the deformed young ice part there is no clear co-polarization signal separating it from the surrounding sea ice in C-band.

Studies by [1] using C-band scenes and an incidence angle of 35.0^o show co-polarization ratio values of 3 dB for dark nilas and -2 dB for bright nilas. The type of young ice may therefore be important for the sign of the co-polarization ratio value. However, the absolute co-polarization value may be similar. In [10] they found that thin ice in C-band corresponded to co-polarization val-

Table 5: Mean co-polarization ratio and mean entropy values for the young ice class. For May 26 two satellite scenes for each of the different wavelengths make up the dataset. They are here denoted as the lower (L) and upper (U) scenes referring to the relative position seen in Fig. 1.

Pair #	**Satellite**	**Date**	**Co-pol (dB)**	**Entropy**	**Alpha**	**Sigma$_{HH}$ (dB)**	**Sigma$_{VV}$ (dB)**
1	Radarsat-2	2015-04-23	-0.19±1.55	0.52±0.09	25.57±4.10	-15.35±2.49	-15.60±2.23
	Radarsat-2	2015-04-23	-0.35±1.11	0.50±0.07	23.27±3.90	-14.80±2.24	-15.15±2.16
	ALOS-2	2015-04-23	1.92±1.36	0.53±0.20	27.74±9.03	-22.14±4.39	-20.23±4.89
2	Radarsat-2	2015-04-28	2.84±1.97	0.54±0.09	31.64±4.28	-21.28±3.83	-18.44±3.18
	ALOS-2	2015-04-28	2.10±1.36	0.51±0.23	28.83±9.38	-23.98±4.35	-21.88±5.14
3	Radarsat-2	2015-05-26(L)	3.39±1.37	0.69±0.08	37.32±4.37	-26.83±1.22	-23.25±1.52
	ALOS-2	2015-05-26(L)	2.94±2.08	0.42±0.16	25.07±3.75	-21.38±1.75	-18.44±2.96
4	Radarsat-2	2015-05-26(U)	2.41±1.53	0.76±0.08	40.86±4.73	-26.65±1.14	-24.42±1.76
	ALOS-2	2015-05-26(U)	0.76±1.14	0.78±0.09	42.36±7.50	-26.55±2.08	-25.79±2.26
5	Radarsat-2	2015-05-31	2.67±1.47	0.55±0.14	29.45±7.04	-25.04±1.97	-22.37±2.51
	ALOS-2	2015-05-31	3.82±1.67	0.42±0.15	26.02±4.15	-23.40±1.89	-19.58±2.88

ues between 1.3 dB and 2.8 dB. Their study was carried out under similar meteorological conditions as the April scenes and at roughly the same time of the year. In [16] they measured a co-polarization ratio of 1 dB for new ice and an incidence angle of 30^o, and a co-polarization ratio of 2 dB for an incidence angle of 40^o. Using an incidence angle of 52.5^o [3] found for thin ice a co-polarization ratio range from 3 dB to 8 dB for C-band SAR. Their meteorological conditions were similar to the conditions for the May scenes and were carried out in the freeze-up period. The co-polarization ratio in our study is also comparable with the values measured in May with an incidence angle of 49.0^o.

The L-band scenes have mean co-polarization ratios of 1.92 dB up to 2.94 dB. The exception from this is the scene from May 26 (upper) where the mean co-polarization ratio value is 0.76 dB. The positive co-polarization values are in line with results in [22] and [7]. In [7] they showed that in L-band data the co-polarization ratio was higher for new ice in leads than the surrounding sea ice. In the scenes used in this study the leads are clearly identifiable within the individual satellite scene using the co-polarization ratio. The study by [7] was carried out under similar meteorological conditions and with a similar incidence angle as for our study in April. Studies by [7] also showed that the young ice has a larger range for backscatter intensity values and may therefore be difficult to separate from level first year ice. It may therefore be beneficial to include the surface scattering mechanisms to separate the younger ice from other sea ice as well as open water areas. In [21] they observed that in L-band scenes scattering entropy over thin sea ice is higher than over thicker sea ice. The mean scattering entropy was found to be 0.75 ± 0.04 for thin ice areas for incidence angles from 23^o to 25^o. In [19] they showed that thin ice in L-band scenes has scattering entropy values higher than 0.4 when the incidence angles ranges from 20^o to 30^o. This is in line with the values observed in our study (Tab. 5) for both C- and L-band, although the variability in our results is greater than for their study. The mean Sigma$_{VV}$ values of -21.82 dB observed in their study for L-band data are in line with the values observed in this study. The wind speed was lower in case of the two datasets used in [21], 3.2 m/s and 4.6 m/s respectively than for any of the satellite scenes used here (Tab. 3).

The observed open water leads on April 23 have in the C- and L-band data low entropy values ($\sim$0.3) and the leads where *in-situ* data confirm the ice type as young ice have high values of $\sim$0.65-0.8. The results presented in Tab. 5 are an average of these values. For the L-band scene on April 23 the level part of the lead has relatively high scattering entropy values of 0.8 and the deformed part has values of 0.6. For the C-band data no such clear trend can be observed. Higher entropy values are interpreted as having more complex scattering mechanisms. In [21] they argue that thin ice generally has higher entropy values than thicker sea ice. Despite differences in wind speed between [21] and our study (Tab. 3) the observed entropy and α values are comparable. Dependence on wind speed, however, can only be expected for open leads.

For the scenes from April the low (high) entropy values are linked to lower (higher) α values. In the C-band scenes the α values indicate that young ice leads have a value of $\sim$30 and that the open water leads have a value of $\sim$10. In the L-band scenes the open water α values are close to 0 and the young ice has values of approximately 50. Moreover, the leads that appear to be the youngest on April 23 have a value between the two but closer to the open water value. For the lead where *in-situ* data confirm one part deformed young ice and another part level young ice the α values are for the deformed part $\sim$40 and for the level part $\sim$50. Both the α and the scattering entropy mean values will be affected by the inclusion

of open water leads. From the α values the dominating type of scattering mechanism can be interpreted. Surface scattering is represented by low values, volume scattering by intermediate values, and double bouncing by high values [4]. However, [14], showed that increased scattering entropy values may also be associated with signal values close to the noise floor. For the C-band scenes in May the cross-pole channels are close to the NESZ in the leads. The overall entropy and α values for the C-band scenes are higher in May than for April.

5. CONCLUSION

In the C-band scenes used here a co-polarization ratio value of approximately -2 dB or 2 dB indicate young sea ice or open water. Inclusion of scattering entropy and α values enables easier separation from both the surrounding sea ice and open water. Entropy values $>$0.4 and α values $>$30 indicate young ice areas. For the L-band scenes co-polarization values of $>$1.9 dB, entropy values $>$0.4 and α values $>$50 could be used to separate the young ice from the surrounding sea ice and open water.

6. ACKNOWLEDGEMENT

The ALOS-2 Palsar-2 scenes were provided by JAXA under the 4th Research Announcement program. Radarsat-2 data is provided by NSC/KSAT under the Norwegian-Canadian Radarsat agreement 2015. This work has been supported by the Norwegian Polar Institutes Centre for Ice, Climate and Ecosystems (ICE) through the N-ICE project. The work as been supported by the Norwegian Research Council, through the NORRUSS program and by CIRFA Centre for Integrated Remote Sensing and Forecasting for Arctic Operations. The authors wish to thank the personnel from the Norwegian Polar Institute as well as other organisations, the R/V Lance crew and the Airlift AS helicopter crew who participated in the field work campaign N-ICE2015. A.P. Doulgeris is gratefully acknowledged for the assistance with the segmentation algorithm. P. Wagner is gratefully acknowledged for the sea ice classification.

REFERENCES

[1] Beaven, S.G., Gogineni, S.P. & Shanableh, M. (1993). Young sea ice signatures in the deep Arctic during the fall freeze-up. *Geosci. and Rem. Sens. Symp., IGARSS '93*. **2**, 434–436. doi:10.1109/IGARSS.1993.322312

[2] Brigham, L.W. (2010). The fast-changing maritime Arctic. *U.S. Naval Institute Proceedings*. **136**(5), 54–59.

[3] Brath, M., Kern, S. & Stammer, D. (2013). Sea Ice Classification During Freeze-Up Conditions With Multifrequency Scatterometer Data. *IEEE Trans. Geosci. Rem. Sens.*. **51**(6), 3336–3353. doi:10.1109/TGRS.2012.2222

[4] Cloude, S.R. & Pottier, E. (1997). An entropy based classification scheme for land applications of polarimetric SAR. *IEEE Trans. Geosci. Rem. Sens.*. **35**(1), 68–78. doi:10.1109/36.551935

[5] Dierking, W. & Busche, T. (2006). Sea ice monitoring by L-band SAR: An assessement based on literature and comparisons of JERS-1 and ERS-1 imagery. *IEEE Trans. Geosci. Rem. Sens.*. **44**(2), 957–979. doi:10.1109/TGRS.2005.861745

[6] Dierking, W. (2010). Thin ice classification and thickness estimation using ASAR, Palsar, Radarsat-2, and Terrasar-X data: First results. *In Proc. of ESA Living Planet Symposium, Bergen, Norway, 2010, ESA SP-686 (CD-ROM), ESA Publications Division, European Space Agency, Noordwijk, The Netherlands.*

[7] Dierking, W. (2010b). Mapping of Different Sea Ice Regimes Using Images From Sentinel-1 and ALOS Synthetic Aperture Radar. *IEEE Trans. Geosci. Rem. Sens.*. **48**(3), 1045–1058. doi:10.1109/TGRS.2009.2031806

[8] Doulgeris, A.P. & Eltoft, T. (2010). Scale mixture of Gaussian modelling of polarimetric SAR data. *EURASIP J. Appl. Signal Proc.*. **874592**. doi:10.1155/2010/8745

[9] Doulgeris, A.P. (2013). A Simple and Extendable Segmentation Method for Multi-Polarisation SAR Scenes. *Proc. POLinSAR 2013, Frascati, Italy*.

[10] Geldsetzer, T. & Yackel, J. J. (2009). Sea ice type and open water discrimination using dual co-polarized C-band SAR. *Can. J. Rem. Sens.*. **35**(1), 73–84. doi:10.5589/m08-075

[11] Granskog, M.A., Assmy, P., Gerland, S., Spreen, G., Steen, H. & Smedsrud L.H. (2016). Arctic research on thin ice: Consequences of Arctic sea ice loss. *Eos*. **97**. doi:10.1029/2016EO044097

[12] Gupta, M., Scharien, R. K. & Barber, D.G. (2013). C-Band Polarimetric Coherences and Ratios for Discriminating Sea Ice Roughness, *Int. J. of Oceanography*, **2013**. doi:10.1155/2013/567182

[13] Haas, C., Lobach, J., Hendricks, S., Rabenstein, L. & Pfaffling, A. (2009). Helicopter-borne measurements of sea ice thickness, using a small and lightweight, digital EM system. *J. of Appl. Geophys., Airborne Geophysics*. **67**, 234–241. doi:10.1016/j.jappgeo.2008.05.005

[14] Minchew, B., Jones, C. E. & Holt, B. (2012). Polarimetric analysis of backscatter from the Deepwater Horizon oil spill using L-band synthetic aperture radar. *IEEE Trans. Geosci. Rem. Sens.*. **50**(10), 3812–3830. doi:10.1109/TGRS.2012.2185804

[15] Moen, M.-A.N., Doulgeris, A.P., Anfinsen, S.N., Renner, A.H.H., Hughes, N., Gerland, S. & Eltoft, T. (2013). Comparison of automatic segmentation of full polarimetric SAR sea ice scenes with manually drawn ice charts. *The Cryosphere*. **7**(6), 1693–1705. doi:10.5194/tc-7-1693-2013

[16] Onstott, R.G. (1992). SAR and Scatterometer Signatures of Sea Ice Chapter 5, *In: Carsey FD (ed) Microwave remote sensing of sea ice. American Geophysical Union, Washington D.C.*. 77–104.

[17] Renner, A.H.H., Hendricks, S., Gerland, S., Beckers, J., Haas, C. & Krumpen, T. (2013). Large-scale ice thickness distribution of first-year sea ice in spring and summer north of Svalbard. *Annals of Glaciology*. **54**, 13–18. doi:10.3189/2013AoG62A146

[18] Ressel, R. & Singha, S. (2016). Comparing Near Coincident Space Borne C and X Band Fully Polarimetric SAR Data for Arctic Sea Ice Classification. *Rem. Sens.*. **8**(3), 198. doi:10.3390/rs8030198

[19] Wakabayashi, H., Matsuoka, T., Nakamura, K. & Nishio, F. (2004). Polarimetric characteristics of sea ice in the Sea of Okhotsk observed by airborne L-band SAR. *IEEE Trans. Geosci. Rem. Sens.*. **42**(11), 2412–2425. doi:10.1109/TGRS.2004.836259

[20] Wakabayashi, H. & Sakai, S. (2010). Estimation of sea ice concentration in the sea of Okhotsk using Palsar polarimetric data. *Proc. of Int. Geosci. and Rem. Sens. Symp.*. 2398–2401.

[21] Wakabayashi, H., Mori, Y. & Nakamura, K. (2013). Sea Ice Detection in the Sea of Okhotsk using PALSAR and MODIS data, *IEEE J. Selected. Topics. Appl. Earth. Obs. and Rem. Sens.*. **6**(3), 1516–1523. doi:10.1109/JSTARS.2013.2258327

[22] Winebrenner, D.P., Farmer, L.D. & Joughin I.R. (1995). On the response of polarimetric synthetic aperture radar signatures at 24-cm wavelength to sea ice thickness in Arctic leads. *Radio Science*. **30**(2), 373–402. doi:10.1029/94RS02313